# Investigating the link between inner gravitational potential and star-formation quenching in CALIFA galaxies

(article starts on next page)

**Astronomy & Astrophysics**

# Investigating the link between inner gravitational potential and star-formation quenching in CALIFA galaxies

V. Kalinova[1], D. Colombo[1], S. F. Sánchez[2], E. Rosolowsky[3], K. Kodaira[1,4,5], R. García-Benito[6], S. E. Meidt[7], T. A. Davis[8], A. B. Romeo[9], S.-Y. Yu[1], R. González Delgado[6], and E. A. D. Lacerda[2]

[1] Max Planck Institute for Radioastronomy, Auf dem Hügel 69, 53121 Bonn, Germany
e-mail: `kalinova@mpifr.de`
[2] Instituto de Astronomía, Universidad Nacional Autonóma de México, A.P. 70-264, 04510 Mexico DF, Mexico
[3] Department of Physics 4-181 CCIS, University of Alberta, Edmonton, AB T6G 2E1, Canada
[4] National Astronomical Observatory of Japan, Osawa2-21-1, 181-8588 Mitaka-shi, Tokyo, Japan
[5] SOKENDAI, International Village, Hayama-machi, 240-0193 Miura-gun, Kanagawa-ken, Japan
[6] Instituto de Astrofísica de Andalucía, CSIC, Apartado de correos 3004, 18080 Granada, Spain
[7] Sterrenkundig Observatorium, Universiteit Gent, Krijgslaan 281 S9, 9000 Gent, Belgium
[8] School of Physics and Astronomy, Cardiff University, Queens Buildings, The Parade, Cardiff CF24 3AA, UK
[9] Department of Space, Earth and Environment, Chalmers University of Technology, 41296 Gothenburg, Sweden

## ABSTRACT

It has been suggested that gravitational potential can have a significant role in suppressing star formation in nearby galaxies. To establish observational constraints on this scenario, we investigated the connection between the dynamics – taking the circular velocity curves (CVCs) as a proxy for the inner gravitational potential – and star formation quenching in 215 non-active galaxies across the Hubble sequence from the Calar Alto Legacy Integral Field Area (CALIFA) survey. Our results show that galaxies with similar CVCs tend to have a certain star-formation quenching pattern. To explore these findings in more details, we constructed kiloparsec(kpc)-resolved relations of the equivalent width of the Hα ($W_{H\alpha}$) versus the amplitude ($V_c$) and shape ($\beta = d \ln V_c/d \ln R$) of the circular velocity at given radii. We find that the $W_{H\alpha} - V_c$ is a declining relationship, where the retired regions of the galaxies (the ones with $W_{H\alpha}$ values of below 3 Å) tend to have higher $V_c$. Concurrently, $W_{H\alpha} - \beta$ is a bimodal relationship, which is characterised by two peaks: concentration of the star forming regions at a positive $\beta$ (rising CVC) and a second concentration of the retired regions with a negative $\beta$ (declining CVC). Our results show that both the amplitude of the CVC – driven by the mass of the galaxies – and its shape – which reflects the internal structure of the galaxies – play an important role in the quenching history of a galaxy.

**Key words.** galaxies: evolution – galaxies: kinematics and dynamics – galaxies: star formation – galaxies: fundamental parameters – galaxies: structure – galaxies: bulges

## 1. Introduction

The transition of a galaxy from blue and young system to one that is red and retired is referred to as the process of 'star-formation quenching' (e.g. Strateva et al. 2001; Faber et al. 2007), and is characterised by a fast decline in star formation rate (SFR; e.g. Corcho-Caballero et al. 2021). Several quenching mechanisms have been proposed to explain the diversity of galaxies we observe today and they can be grouped into external (outside of the galaxy) and internal (within the galaxy).

Environmental quenching (Peng et al. 2010; Gunn et al. 1972; Abadi et al. 1999) is an external process. This includes ram-pressure stripping of the galactic interstellar medium, strangulation (removal of the outer gaseous envelope of a galaxy falling into a galaxy cluster, which will cease the star formation of the galaxy as the only available gas is hot and cannot replenish its cold gas reservoir (Larson et al. 1980; Balogh et al. 2000), and galaxy harassment (quenching due to interactions with other members of the galaxy cluster, leading to dynamical heating Farouki & Shapiro 1981; Moore et al. 1996; Bluck et al. 2020a,b). Low-mass galaxies in particular can have their gas removed by tidal stripping during travel towards the centre of a galaxy cluster (e.g. Abadi et al. 1999).

In addition, a large range of internal processes are also thought to be able to quench star formation. Dark matter (DM) halo quenching is considered an internal process, related to the most extended component of the galaxies. In systems with critical DM halo mass of $\sim 10^{12} M_\odot$, the accreted gas is shocked and heated to the virial temperature of the halo, preventing star formation (Birnboim & Dekel 2003). The correlation between the stellar component and the quenching of the massive galaxies is known as mass quenching (Peng et al. 2010). Active galactic nucleus (AGN) feedback quenching is able to suppresses star formation in galaxies (Husemann & Harrison 2018). AGN feedback can transfer radiation to the surrounding gas and suppress gas accretion (Di Matteo et al. 2005), or kinetic energy and momentum can cause expulsion of gas (Croton et al. 2006). The ejective galactic winds from supernovae or HII regions constitute another quenching feedback mechanism (stellar feedback quenching), which acts mostly in low-mass and late-type galaxies (e.g. Colling et al. 2018). Internal dynamics also contribute to the quenching of galaxies. Secular evolution processes can form a bar structure that generates radial inflow towards the centre of the galaxy, increasing the random motion of the gas and the disc heating that stabilises the inner gaseous disc (Romeo & Fathi 2015, 2016; Khoperskov et al. 2018).

Additionally, bars drive gas flow towards the galactic centre, which can trigger a central starburst, which in turn can consume almost all the gas, causing a quenched centre. This action leads to periodic episodes of quenching and star formation at the centre of bars (Krumholz & Kruijssen 2015). The growth of the central spheroid (bulge) seems to play an important role in ceasing the star formation in a galaxy via stabilisation of the disc against gravitational instability, a process known as morphological quenching (Martig et al. 2009), gravitational quenching (Genzel et al. 2014), or dynamical suppression (e.g. Davis et al. 2014; Gensior et al. 2020; Gensior & Kruijssen 2021).

Overall, the causes of star-formation quenching in galaxies are highly complex and still debated. It is not clear whether there is one dominant mechanism or a mixture of several processes that are responsible for the variety of galaxy morphologies seen today. Recent resolved studies tried to disentangle these effects by classifying the galaxies based on their star formation activity (or its absence; Singh et al. 2013; Belfiore et al. 2016; Lacerda et al. 2018). In particular, Kalinova et al. (2021, hereafter K21) distinguish various quenching patterns (referred to as 'quenching stages'; Fig. 1) in the spatially resolved ionised gas distribution of the galaxies, where the ratio of star-forming to quenching regions of the galaxies increases from late-type to early-type galaxy morphologies (e.g. Lacerda et al. 2018, K21). Based on H$\alpha$-equivalent-width ($W_{H_\alpha}$) thresholds (e.g. Sánchez et al. 2014; Lacerda et al. 2020), K21 distinguished star-forming ($W_{H_\alpha} > 6$ Å), mixed ($3 < W_{H_\alpha} \leq 6$ Å), and retired ($W_{H_\alpha} \leq 3$ Å) regions within the field of view of the galaxies. These authors proposed six quenching stages of the systems (see Fig. 1): star-forming (fully dominated by recent star formation), quiescent-nuclear-ring (presence of a quiescent-ring structure in the central regions, but still dominated by star formation in the outskirts), centrally quiescent (quiescent inner region within $0.5R_e$ of the galaxy, where $R_e$ is the effective radius of the galaxy), mixed (no clear patterns in the ionised gas distributions), nearly retired (quiescent galaxies with a few star-formation regions), and fully retired (completely quiescent objects up to $2R_e$).

In this study, we explore the connection between the dynamics and star-formation quenching stage of the galaxies, shedding light on the role of the dynamical suppression mechanism for their formation. To achieve this goal, we compare the circular velocities of the galaxies (tracing the total gravitational potential of the systems; Kalinova et al. 2017, hereafter K17) and the values of $W_{H_\alpha}$ (K21), serving as a star-formation quenching marker across the Hubble sequence.

## 2. Sample and data

Our sample is derived from the 238 CALIFA (Calar Alto Legacy Integral Field Area; Sánchez et al. 2012) survey galaxies, extensively analysed in K17 and K21. It is a representative population of the CALIFA mother sample (see Fig. 1 in K17), and therefore of the nearby Universe galaxies (Walcher et al. 2014). In our analysis, we only discard a few targets: the active galaxy members (15 strong AGN and 8 weak AGN galaxies) from the original sample of K17 and K21 so as to avoid any possible biases due to the presence of nuclear activity in the galaxies. The final sample consists of 215 non-active galaxies, spanning six different quenching stages as defined in K21 (see Fig. 1 of K21 and Fig. 1 of this study), various morphologies (from elliptical to late-type spiral galaxies), stellar masses (from $6 \times 10^8 \, M_\odot$ to $5 \times 10^{11} \, M_\odot$), and redshifts ($0.005 < z < 0.03$). Further details about

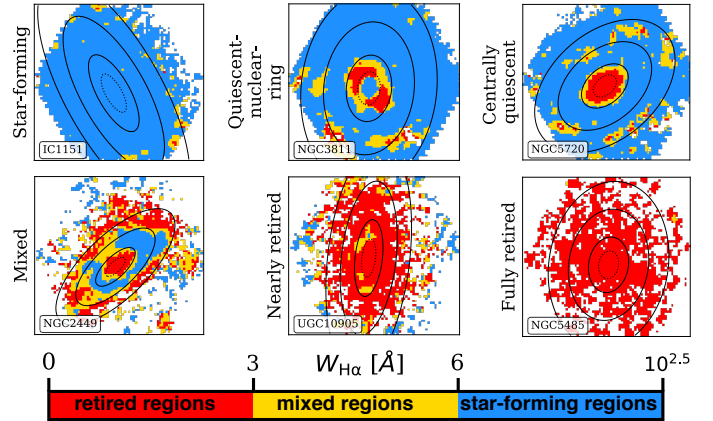**Fig. A.1.** Circular velocity curve classification, shown in the first ro

**Fig. 1.** Example of galaxy quenching stages defined by K21 through visual inspection of the $W_{H_\alpha}$ distribution (*from top left to bottom right*): star-forming, quiescent-nuclear-ring, centrally quiescent, mixed, nearly retired, and fully retired. The colour bar separates the regions of the $W_{H_\alpha}$ maps (e.g. Sánchez et al. 2014, K21) into: star-forming ($W_{H_\alpha} > 6$ Å), mixed ($3 < W_{H_\alpha} \leq 6$ Å), and retired ($W_{H_\alpha} \leq 3$ Å). The dashed contours correspond to half of the galaxy's effective radius ($R_e$), while the continuous contours indicate 1, 2, and $3R_e$. See Sect. 1 and K21 for more details.

the survey and data reduction can be found in Sánchez et al. (2012), Husemann et al. (2013), García-Benito et al. (2015), and Sánchez et al. (2016a).

To perform this study, we use the publicly available circular velocity curve (CVC) catalogue of K17. CVC is defined as $V_c^2(R) = R\frac{\partial\Phi}{\partial R}|_{z=0}$, where $\Phi(R, z)$ is the gravitational potential and $R$ is the galactocentric radius, respectively. Further, the CVC is calculated through the solutions of the axisymmetric Jeans equations by applying the Jeans Axisymmetric Modelling (JAM) code of Cappellari (2008)[1]. First, K17 derive the surface brightness (SB) of the galaxies using the $r$-band images from the Sloan Digital Sky Survey (SDSS)[2] catalogue Data Release 12 (DR12; Alam et al. 2015) through the multi-Gaussian expansion method (MGE; Monnet et al. 1992; Emsellem et al. 1994). Given the defined SB of the galaxies, the second velocity moment of the galaxies ($V_{rms} = \sqrt{V^2 + \sigma^2}$) of the stellar kinematics (based on the high-resolution 'V1200' dataset; Falcón-Barroso et al. 2017) is fitted, assuming constant dynamical mass-to-light ratio ($\gamma_{dyn}$) and constant velocity anisotropy ($\beta_z = 1 - \sigma_z^2/\sigma_r^2$) in the galactic meridional plane. In the end, the CVCs were inferred from the de-projected SB of the galaxies, scaling by the best-fit value of $\gamma_{dyn}$ (see Eq. (3) in K17).

The emission-line analysis for deriving the maps of the equivalent width of the H$\alpha$ line ($W_{H_\alpha}$) was based on the PIPE3D pipeline (Sánchez et al. 2016b,c) calculations, assuming a Salpeter (Salpeter 1955) initial mass function (IMF). Further details about the adopted data and analysis are provided in K17 and K21.

## 3. Results

The results of our first test designed to help us further understand the link between the inner gravitational potential of the galaxies and their quenching stage are presented in Fig. 2. We group the CVCs of the galaxies by their quenching stage using the
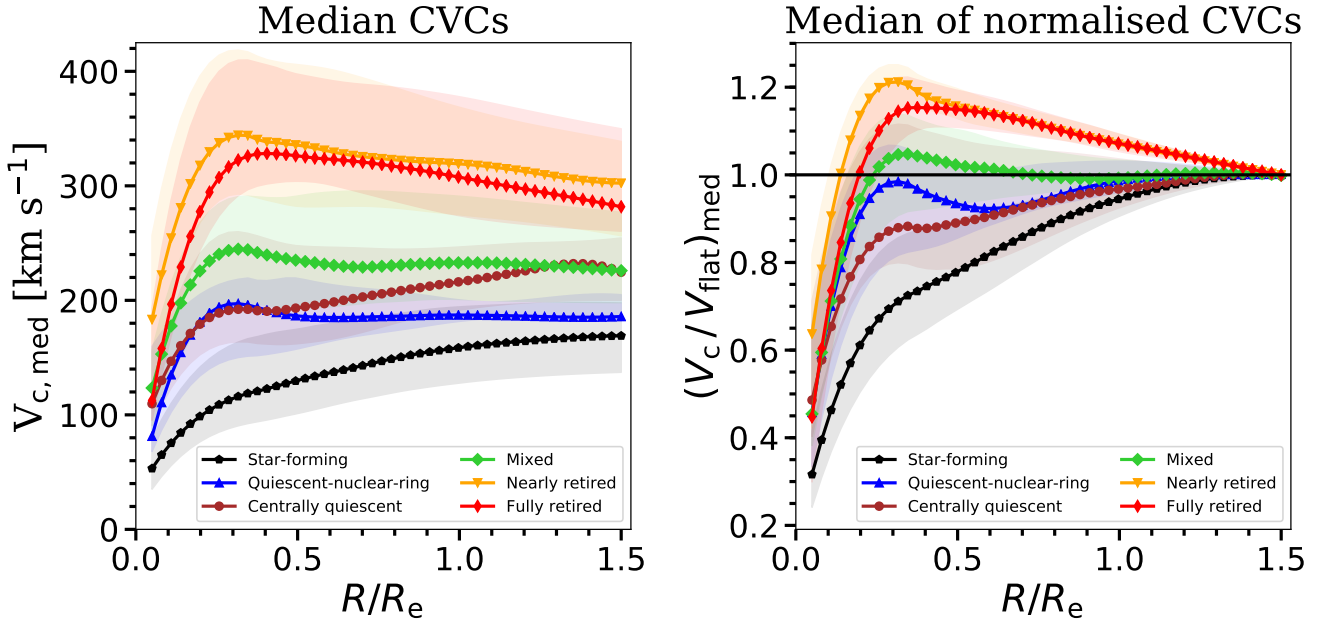
---

[1] http://purl.org/cappellari/software
[2] https://www.sdss.org/

## Median CVCs

## Median of normalised CVCs



**Fig. 2.** Average CVC profiles. *Left*: median curve of the CVC profiles for each quenching stage group from star-forming to fully retired galaxies. *Right*: median of the CVC profiles, normalised with respect to the asymptotic velocity for each quenching-stage group. The uncertainty bands correspond to the 25th percentile (below) and the 75th percentile (above) of the median distribution. To smooth the median CVCs and the percentile profiles, we apply the Savitzky-Golay smoothing filter (Savitzky & Golay 1964) by adopting a third-degree polynomial and a 21-point wide sliding window (see Sect. 3).

CALIFA CVC catalogue of K17. The amplitude and the slope of the central regions ($\sim$0.1–0.4$R_e$) of the median profiles (left panel) increase as the galaxies become progressively more quenched, for example increasing in the following sequence: star-forming; to quiescent-nuclear-ring and centrally quiescent; to mixed; to fully retired; to nearly retired. We notice that in the central region (up to 0.4$R_e$), centrally quiescent systems have similar median velocity to the quiescent-nuclear-ring galaxies, but larger velocity in the outer parts (above 0.4$R_e$). This indicates that the disc of the centrally quiescent galaxies is more massive than that of the quiescent-nuclear-ring systems. On the contrary, in the outer regions (above 0.4$-$0.5$R_e$), the nearly retired galaxies have similar disc median velocity to the fully retired systems, but larger bulge median velocity in the central parts (below 0.4$-$0.5$R_e$). Among all quenching-stage groups, the nearly retired galaxies have the largest central mass concentration (the highest $V_c$-peak). This might suggest that the fully retired systems (or even the rest of the quenching stage galaxies) are progenitors of the nearly retired galaxies (via reignition of star formation and mass build-up by merger events), or that the nearly retired class has followed a different evolutionary path from the other classes. Furthermore, in the right panel of Fig. 2, the median of the CVC profiles, normalised with respect to the asymptotic velocity, reveals a more distinguishable order: star-forming; to centrally quiescent; to quiescent-nuclear-ring; to mixed; to fully retired; to nearly retired. Nevertheless, individually, the curves in a given quenching stage show significant variation. In particular, several star-forming galaxies are characterised by declining profiles, while some retired objects have rising profiles (see also the individual CVCs in each quenching-stage group in Figs. A.1 and A.2).

Figure 2 suggests that, on average, there is a correlation between the CVC shape and amplitude, and quenching stage. To obtain a more detailed quantification of these correlations, we constructed two resolved relationships using the available information from the $W_{H_\alpha}$ maps and CVCs.

### 3.1. Resolved quenching relations

The first relation, quenching–velocity ($W_{H_\alpha} - V_c$), compares the $W_{H_\alpha}$ value and the amplitude of the circular velocity ($V_c$) at a given position in the field of view of the galaxy (i.e. spaxel-by-spaxel). We calculated the circular velocity, $V_c$, value at each radius of the de-projected radial map of the galaxies using the MGE_VCIRC procedure included in the JAM package of Cappellari (2008). The inclination and the MGE models of the galaxies were adopted from K17. Assuming that the galaxies are axisymmetric, we derive 'maps' with constant values of $V_c$ at a given galactocentric radius. Once we obtain the $V_c$ map, we are able to construct the second relationship, quenching−CVC shape ($W_{H_\alpha} - \beta$), where $\beta$ is the derivative of $V_c$ with respect to the radius, $\beta = \mathrm{d}\ln V_c/\mathrm{d}\ln R$. If the rising part of the CVC is close to a solid body rotation, then $V_c \propto R$, giving $\beta = 1$, while if some part of the curve is flat then $V_c = $ constant, and therefore $\beta = 0$. If the logarithmic derivative of the CVC is negative ($\beta < 0$) then the CVC is declining (e.g. Sect. 4.2.4 of Leroy et al. 2008). The statistical robustness of both resolved relationships is demonstrated in Appendix C.

Additionally, we use the Pearson's correlation coefficient[3] ($\rho$; e.g. Kowalski 1972) to test the strength of the monotonically linear relation. The coefficient $\rho$ can vary between +1 and −1 for linear correlation and linear anti-correlation, respectively (where 0 refers to no correlation between the two studied data sets). The Spearman's rank correlation coefficient[4] ($s$; e.g. Zwillinger & Kokoska 1999) tells us whether the tested relationship is monotonically increasing ($s = 1$), monotonically decreasing ($s = -1$), or there is a non-monotonic relationship ($s = 0$) that is independent of its linearity.
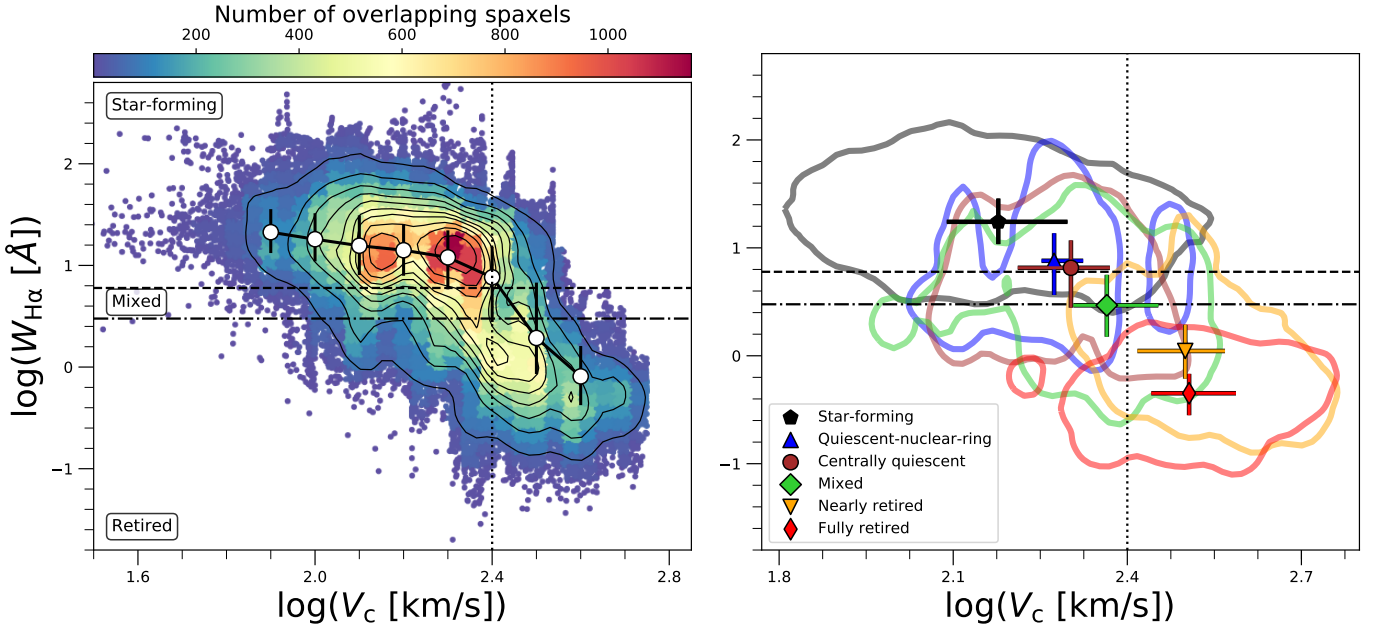
---

[3] https://docs.scipy.org/doc/scipy/reference/generated/scipy.stats.pearsonr.html
[4] https://docs.scipy.org/doc/scipy/reference/generated/scipy.stats.spearmanr.html

**Fig. 3.** CVC amplitude versus $W_\alpha$, which defines the quenching, mixed, and star-forming regions of the galaxies at each position of the sky. *Left panel*: bi-dimensional histograms (colours) overlaid with black contours indicating the regions that contain between 15% and 90% of the total number of points. White circles indicate the sample $W_{H\alpha}$ medians within bins of 0.1 dex, while the vertical black bars encompass the 25th to the 75th percentiles of the distributions within the bins. (We note that the estimated median values do not generally correspond to the peaks of the spaxel distribution indicated by the redder colours or by the contour levels because of the non-Gaussian distributions of the $W_{H\alpha}$ values within given $V_c$ bins.) The colour bar indicates the number of the overlapping spaxels. *Right panel*: coloured contours contain 95% of the data points within a given quenching stage. With the same colours, the markers indicate the positions of the medians of the $W_{H\alpha}$ and $V_c$ distributions of each stage, while the coloured bars mark the extension of the distributions within the 25th and 75th percentiles. Dashed-dotted and dashed black horizontal lines indicate the positions of $W_{H\alpha} = 3$ Å and $W_{H\alpha} = 6$ Å, respectively. The vertical dotted line marks the critical velocity of $\log(V_c) \sim 2.4$ km s$^{-1}$ ($V_c \sim 250$ km s$^{-1}$) at which the relation starts to steepen.

The resolved quenching–velocity relation, $W_{H\alpha} - V_c$, which includes all values of the spaxels in each galaxy of our sample is displayed in Fig. 3 (left panel). Generally, the two quantities are moderately correlated ($\rho = -0.62$ and $s = -0.60$) with high significance (for both coefficients, we obtained a $p$-value $\ll 0.01$, indicating that the moderate correlation between the two quantities is not due to chance). The relation presents two slopes, as it flattens in low velocities and steepens in the high velocities above the critical value $\log(V_c) \sim 2.4$ km s$^{-1}$ ($V_c \sim 250$ km s$^{-1}$). Overall, the retired spaxels (i.e. those with $W_{H\alpha} < 3$ Å) tend to be characterised by higher circular velocities. Furthermore, if we segregate the quenching–velocity relation into the six quenching stages (right panel of Fig. 3; see also Fig. B.1), we observe a smooth transition from star-forming to fully retired galaxies from the top-left (high $W_{H\alpha}$ and low $V_c$) to the bottom-right (low $W_{H\alpha}$ and high $V_c$) side of the relation. The central regions of the relation ($\log(W_{H\alpha}) \sim 1$ Å and $\log(V_c) \sim 2.3$ km s$^{-1}$) are occupied by the mixed group of galaxies, which are actually green valley galaxies on the way to being fully quenched (see Fig. 11 of K21).

In Fig. 4, the $W_{H\alpha}$ and $\beta$ values moderately correlate ($\rho = 0.49$ and $s = 0.48$), as for the previous relation, with high significance ($p$-value $\ll 0.01$ for both tests). Contrary to the $W_{H\alpha} - V_c$ relation, the $W_{H\alpha} - \beta$ relation is bimodal and characterised by two clear peaks, where one of them is located at $\beta \sim -0.25$ and $W_{H\alpha} \sim 1$ Å, and the second one is located at $\beta \sim 0.25$ and $W_{H\alpha} > 6$ Å, indicating that generally star forming regions are characterised by rising rotation curves, while retired regions are characterised by declining profiles.

We also divided the $W_{H\alpha} - \beta$ diagram across the six quenching stages (see right panel of Figs. 4 and B.2). There is a smooth

transition from fully retired to star-forming galaxies from the bottom-left (low $W_{H\alpha}$ and negative $\beta$) to the top-right side (high $W_{H\alpha}$ and positive $\beta$) of the relation. The intermediate quenching stage spaxel distribution of the mixed galaxies is centrally located at the $W_{H\alpha} - \beta$ plane because of the large fraction of flat CVCs that these systems possess (see Figs. 2, A.1). In particular, the nearly retired and fully retired quenching stage galaxies are almost fully located in the quenched region with declining CVC of the $W_{H\alpha} - \beta$ diagram (i.e. $W_{H\alpha} < 3$ Å and $\beta < 0$).

### 3.2. Nature of the scatter in the quenching relations

In the previous section, the $W_{H\alpha} - V_c$ relation depicts a link between quenching and the amplitude of CVCs, showing in particular that the majority of spaxels with high velocity (i.e. $V_c \sim 250$ km s$^{-1}$) are quenched (i.e. $W_{H\alpha} < 3$ Å). The $W_{H\alpha} - \beta$ relation, meanwhile, highlights the connection between quenching and the shapes of CVCs and exhibits a clear bimodality: whereas star forming regions are overall characterised by rising curves, quenched regions are associated with decreasing curves.

Both quenching relations exhibit a large level of scatter; however, in the $W_{H\alpha} - V_c$ plane, quenched regions can also arise at low circular velocity and there are a large number of star-forming regions at high velocity. Many outlier spaxels in the $W_{H\alpha} - \beta$ relation represent star-forming regions with declining curves, whereas others are quenched regions with rising curves.

In this section, we present the results of a test designed to reveal whether these outliers are related to the global
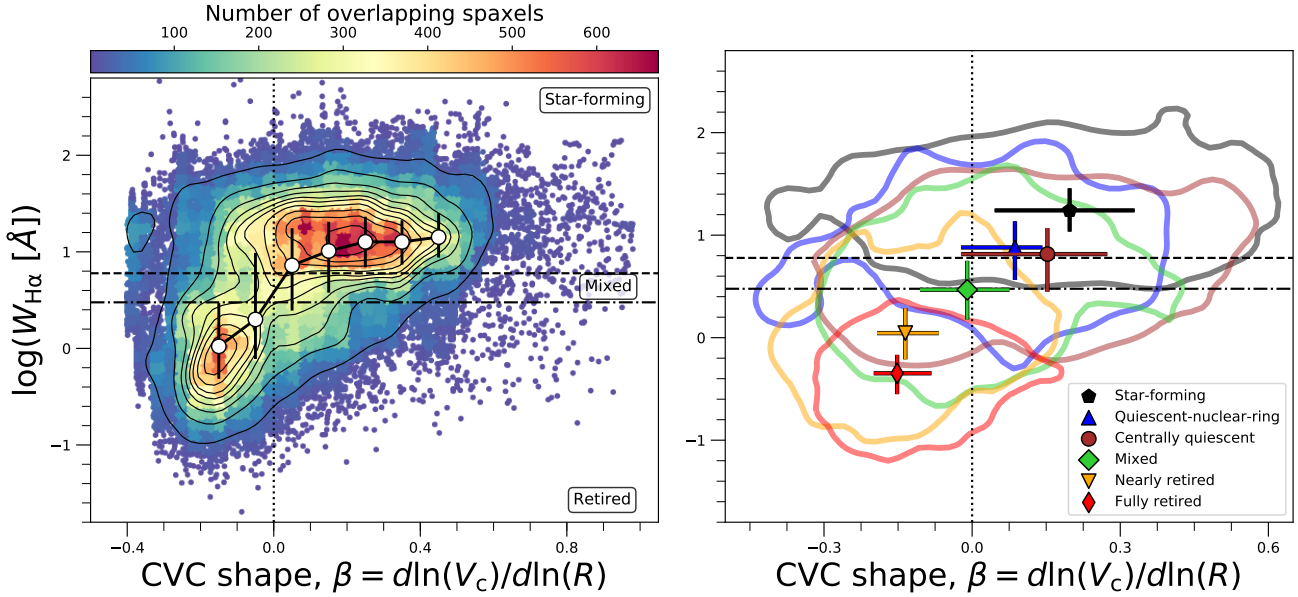
**Fig. 4.** Quenching versus shape of the CVC measured through $\beta = d \ln V_c / d \ln R$, the value of which we infer for each pixel of the radial and circular velocity maps. The rising part of the curve behaves as a solid body, $V_c \propto R$, giving $\beta = 1$, while in the flat part of the curve, $V_c$ = constant, and $\beta = 0$ (vertical dotted line). Negative values of the logarithmic derivative ($\beta < 0$) correspond to the declining part of the CVC. Symbols and conventions follow Fig. 3.

morphologies of the galaxies in our sample. Indeed, morphological features such as bulges, bars, and spiral arms are important galactic dynamical structures (see Sect. 4). We examined how the observed spaxels are distributed with respect to several indicators of galactic structure including Hubble type, presence of a bar, and bulge nature (e.g. classical or pseudo bulge, Kormendy & Kennicutt 2004; see also Figs. 5 and 6 of this work).

Following, K21 we adopt the Hubble type classifications for the galaxies in our sample from Walcher et al. (2014). As discussed in K21 (see their Fig. 7), late-type spiral galaxies (Sb−Sdm) mostly make up the star-forming class while early-type spirals (Sab−Sbc) predominantly make up the quiescent-nuclear-ring and centrally quiescent galaxies. The mixed quenching stage includes a large variety of morphologies (covering early-type spirals, lenticulars, and ellipticals). The nearly and fully retired galaxies consist only of early-type galaxies (both lenticulars and ellipticals).

According to the bar-type statistics of K21, the quiescent-nuclear-ring group contains the largest number of barred galaxies, followed by centrally quiescent, mixed, and star-forming quenching stages. The nearly- and fully retired groups, on the other hand, mostly consist of unbarred galaxies (see their Fig. 8). It is notable that the quiescent-nuclear-ring, centrally quiescent, and mixed quenching stages consist of early-type spiral galaxies (both lenticulars and discy ellipticals). These systems are therefore dominated by secular evolution and dynamical features (e.g. spiral arms and bars; K21), and we expect these galaxies to be the largest contributor to the scatter in the two trends revealed in this work.

Additionally, we use the central stellar mass surface density of the galaxies within 1 kpc, $\Sigma_{1\,\text{kpc}}$. This parameter has been used as a proxy for both the mass and compactness of the central region (bulge or spheroid) of the galaxies, scaled on the same physical size (Cheung et al. 2012; Luo et al. 2020 and references therein).

For each galaxy, we define $\Sigma_{1\,\text{kpc}} \equiv \frac{M_{*,<1\,\text{kpc}}}{\pi R_{1\,\text{kpc}}^2}$, where $M_{*,<1\,\text{kpc}}$ is the stellar mass of the galaxy integrated within the 1 kpc ellipsoid (obtained by de-projecting the radial map on the plane of the galaxy) and $R_{1\,\text{kpc}} \equiv 1$ kpc (e.g. Cheung et al. 2012). For each galaxy, the stellar mass in a given spaxel is determined from the stellar mass surface density map ($\Sigma_*$, included in the PIPE3D dataset; Sánchez et al. 2016b,c) multiplied by the area of the spaxel. Using $\Sigma_{1\,\text{kpc}}$, we adopt the method of Luo et al. (2020) to classify the central stellar concentration of the galaxies as either 'classical bulges' (CBs) or 'pseudo bulges' (PBs). (Elliptical galaxies are omitted from the bulge classification analysis and are designated with the label 'E' in the bulge statistics of Figs. 5 and 6.) Following Luo et al. (2020), we use the residual $\Delta\Sigma_{1\,\text{kpc}}$ from their measured relation between $\Sigma_{1\,\text{kpc}}$ and global stellar mass ($M_*$, calculated integrating across the entire stellar mass map; Eq. (2) of Luo et al. 2020) to classify galaxies as classical bulge hosts (or elliptical galaxies) when $\log(\Delta\Sigma_{1\,\text{kpc}}) > 0$ and as pseudo bulge hosts when $\log(\Delta\Sigma_{1\,\text{kpc}}) < 0$ (see Luo et al. 2020; their Fig. 7).

As a basic classification of the outliers around the general trend in $W_{H_\alpha}$ versus $V_c$ (Fig. 5), we define a critical velocity $\log(V_c) \sim 2.4$ km s$^{-1}$ ($V_c \sim 250$ km s$^{-1}$) where the trend changes from relatively flat (in the low $V_c$ region) to steep (in the high $V_c$ region). Across this critical value, galaxies also separate broadly into star-forming and quenched groups. Most of the spaxels in the low $V_c$ region ($<250$ km s$^{-1}$) belong to disc galaxies (S0−Sdm) without a dominant bar type (barred, unbarred or unsure) whereas most of the spaxels in the high $V_c$ ($>250$ km s$^{-1}$) zone, on the other hand, come from early-type and unbarred galaxies (E1−Sab).

The critical velocity also tends to mark a separation in the behaviour of $\Sigma_{1\,\text{kpc}}$. For spaxels in the high-$V_c$ region (e.g. mainly above $10^{10}\, M_\odot$ kpc$^{-2}$), $\Sigma_{1\,\text{kpc}}$ is also high independent of whether the region is star-forming or quenched. This indicates that regions with high $V_c$ amplitudes are also those with high central stellar mass density. In the low-$V_c$ regime (e.g.
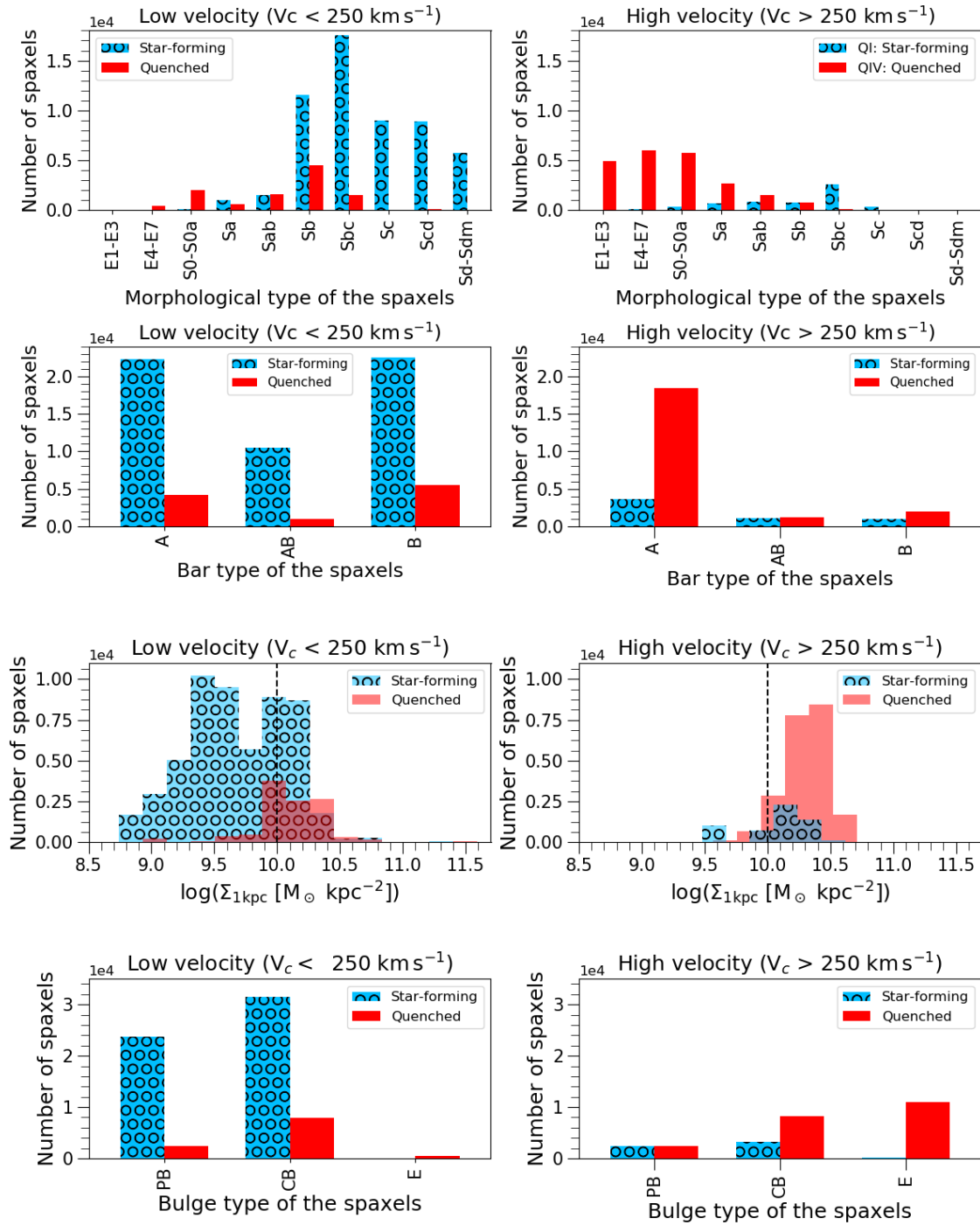
**Fig. 5.** Spaxel distribution of $W_{H\alpha} - V_c$ relation across properties of the host galaxies. The *first* and the *second row panels* correspond to the morphological and bar-type (A: no bar, B: bar, and AB: unsure bar) classifications of the galaxies from Walcher et al. (2014), respectively. The *third row panels* explore the central stellar mass surface density (Sánchez et al. 2016b,c) within 1 kiloparsec ($\Sigma_{1kpc}$) of the host galaxies, following Cheung et al. (2012). *The fourth row panels* relates to the bulge type of the host galaxies, according to the method described in Luo et al. (2020, PB: pseudo bulge, CB: classical bulge, and E: ellipticals). *The left column panels* explore the statistics of the spaxels for low velocities ($V_c < 250$ km s$^{-1}$), while the *right panels* correspond to the high velocities ($V_c > 250$ km s$^{-1}$). The different colours and symbols of the bars distinguish star-forming (blue with black circle) and quenched (red with no symbol) regions of the galaxies. The dashed horizontal lines at $\Sigma_{1kpc} = 10^{10} M_\odot$ kpc$^{-2}$ are drawn to guide the eye. See more details in Sect. 3.2.

mainly below $10^{10} M_\odot$ kpc$^{-2}$), in contrast, only quenched regions have high $\Sigma_{1kpc}$, whereas the star-forming spaxels exhibit a broad bimodal distribution. The broadness of the $\Sigma_{1kpc}$ distribution for this latter subset of galaxies reveals a large variety of central stellar concentrations, and the bimodality tends to correlate with bulge classification, in the sense that star-forming regions can arise in galaxies that host both classical bulges (with high $\Sigma_{1kpc}$) and pseudo bulges (with low $\Sigma_{1kpc}$). Quenched regions are almost exclusively hosts of classical bulges.
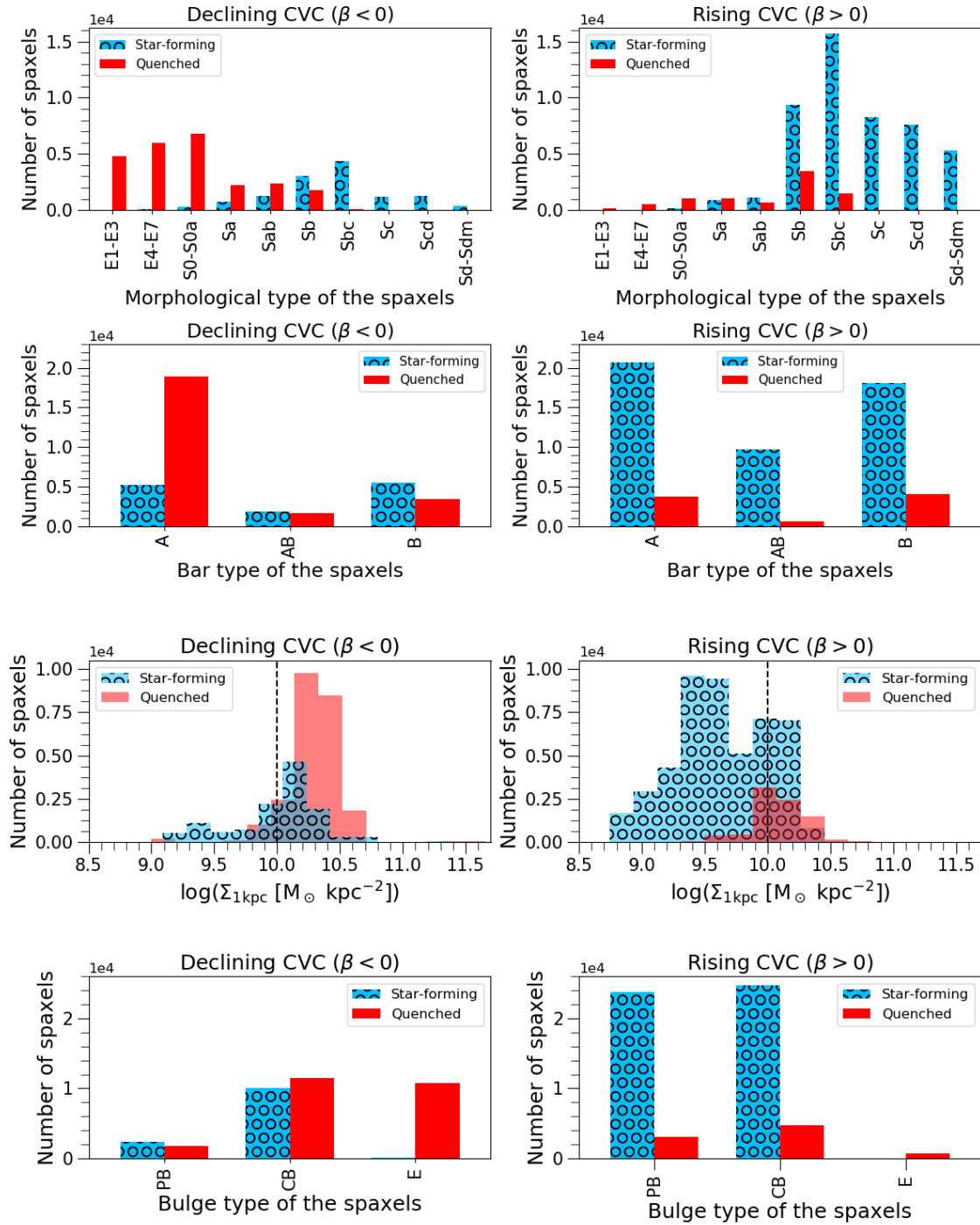
**Fig. 6.** Spaxel distribution of $W_{H\alpha} - \beta$ relation across properties of the host galaxies. *First and the second row panels* correspond to the morphological and bar-type (A: no bar, B: bar, and AB: unsure bar) classifications of the galaxies from Walcher et al. (2014), respectively. *Third row panels* explore the central stellar mass surface density (Sánchez et al. 2016b,c) within 1 kiloparsec ($\Sigma_{1\,kpc}$) of the host galaxies, following Cheung et al. (2012). *Fourth row panels* relates to the bulge type of the host galaxies, according to the method described in Luo et al. (2020, PB: pseudo bulge, CB: classical bulge, and E: ellipticals). *Left column panels* explore the statistics of the spaxels for the declining CVCs ($\beta < 0$), while the *right panels* correspond to the rising CVCs ($\beta > 0$). The different colours and symbols of the bars in the panels distinguish star-forming (blue with black circle) and quenched (red with no symbol) regions of the galaxies. The dashed horizontal lines at $\Sigma_{1kpc} = 10^{10}\,M_\odot\,kpc^{-2}$ are drawn to guide the eye. See more details in Sect. 3.2.

In the $W_{H\alpha} - \beta$ diagram, we see that the majority of the spaxels again separate into two main areas: a star-forming−rising CVC zone ($W_{H\alpha} > 6$ Å and $\beta > 0$) and a quenched−declining CVC region ($W_{H\alpha} < 3$ Å and $\beta < 0$). In other words, the CVCs of the star-forming galaxies are generally slowly rising ($\beta > 0$), while

the CVCs of the quenched systems have a faster inner rise, followed by either a flattened part or a slowly declining part (with $\beta < 0$; outside a central peak caused by a central mass concentration). The star-forming−rising CVC zone is largely populated by spaxels of late-type spirals (Sb−Sdm), both barred and unbarred,

while the quenched−declining CVC region is populated by the spaxels of early-type galaxies (E1−Sb), mostly without bars. This behavior generally agrees with the idea that galactic regions with high stellar mass concentrations (bulges or spheroids) are quenched (e.g. Martig et al. 2009; Gensior et al. 2020).

However, there are significant outliers from these general trends, with some star-forming galaxies exhibiting declining CVCs ($W_{H_\alpha} > 6$ Å and $\beta < 0$) and some quenched galaxies exhibiting rising CVCs ($W_{H_\alpha} < 3$ Å and $\beta > 0$); though we note that these outliers represent only a minority of the sample. Inspection of the individual CVCs in these cases (and across all quenching stages; see Figs. A.1 and A.2) indicates that this quenched subset (of nearly and fully retired class galaxies) are lacking peaks in their CVCs while the subset of star forming galaxies have prominent peaks in their CVCs (e.g. prominent bulges). The latter are found to arise predominantly in classical bulge hosts. (In this same zone, quenched regions are also dominated by ellipticals and classical bulges.) Nevertheless, we note that for both star-forming and quenched regions, rising CVCs are found in galaxies with both classical and pseudo bulges.

Another characteristic of these two outlier regions is that the median of the spaxel distributions is shifted towards early-type disc galaxies (S0−Sbc), both with and without bars (Fig. 6). The $\Sigma_{1kpc}$ spaxel distribution also tends to be tighter compared to the broad distribution characteristic of the star-forming−rising CVC zone.

## 4. Concluding remarks

In this paper, we explore the link between the inner gravitational potential of 215 (E−Sdm) non-active CALIFA galaxies – using their circular velocity curve (CVC) calculated from stellar dynamics within $1.5R_e$ as a proxy for gravitational potential – and their star-formation quenching parameter given by the value of the equivalent width of $H_\alpha$ ($W_{H_\alpha}$). Our main findings can be summarised as follows:

(i) Galaxies with certain CVC shape and amplitude tend to be associated with a specific quenching-stage group.

(ii) There is a moderate correlation between the amplitude of the velocity of the spaxels ($V_c$) and their quenching-proxy values ($W_{H_\alpha}$), where the relationship steepens at higher amplitudes above $\log V_c \sim 2.4$ km s$^{-1}$ ($V_c \sim 250$ km s$^{-1}$).

(iii) The relation between the shape of the CVC ($\beta$) and $W_{H_\alpha}$ is moderate and bimodal, showing that the quenching regions of the galaxies (where $W_{H_\alpha}$ is below 3 Å) are overall characterised by high $V_c$ and negative $\beta$ (declining CVC), and the star-forming regions (where $W_{H_\alpha}$ is above 6 Å) are overall characterised by low $V_c$ and positive $\beta$ (rising CVC).

(iv) The outlier spaxels of the $W_{H_\alpha} - \beta$ relation are largely coming from early-type disc galaxies (S0−Sbc) and follow the opposite trend of the main spaxel distribution, described above.

(v) The spaxels of the nearly and fully retired class galaxies almost fully occupy the quenched−declining CVC region of the $W_{H_\alpha} - \beta$ relation (where $W_{H_\alpha} < 3$ Å and $\beta < 0$).

These findings indicate an important link between the gravitational potential and the present-day star-formation quenching stages of the galaxies. The quenching spaxels lay in regions of the galaxies with a large gravitational potential due to a mass concentration (e.g. bulge or spheroid, bar, and rings). Star formation quenching regulated by gravitational potential is generally referred to as 'dynamical suppression' (or 'morphological quenching' Martig et al. 2009; Genzel et al. 2014; Gensior et al. 2020; Gensior & Kruijssen 2021). Our results support such a

scenario, as we find that a proxy for quenching (e.g. $W_{H_\alpha}$) appears correlated with quantities that trace features of the galactic potential, namely circular velocity curve amplitude ($V_c$) and shape ($\beta$).

A number of other studies have argued that reductions in star formation efficiency (SFE) are responsible for quenching observed in galaxies globally and/or locally (see, e.g. Colombo et al. 2018, 2020; Ellison et al. 2020). In particular, a link between reduced SFE, morphology, increased circular velocity, and rotation curve shear (expressed through the Oort constant $A = 0.5V_c/R(1 - \beta)$) was observed by Colombo et al. (2018) within a sample of galaxies with largely similar molecular gas mass surface densities. That study supports the idea that high shear contributes to the stabilisation of gas discs, preventing fragmentation in the molecular gas (e.g. Toomre 1964; Romeo & Mogotsi 2017) and reducing the rate of star formation (e.g. Martig et al. 2009; Meidt et al. 2013, 2018; Davis et al. 2014).

In addition to shear due to differential rotation (inferred from the CVCs), other kinds of shear may be present due to local gas flows (e.g. Meidt et al. 2018) associated with either spiral arms (Dobbs & Baba 2014; Meidt et al. 2013) or bars (Athanassoula 1992; Sormani et al. 2015). According to a recent analytical model, local and global (orbital) motions in the galactic potential can lead to a dynamical suppression of star formation on the scales of star-forming giant molecular clouds (Meidt et al. 2018, 2020; Liu et al. 2021). In this 'bottleneck' model, galactic orbital motions compete with gas self-gravity on cloud scales. These motions contribute to the velocity dispersion within clouds, thus increasing their stable mass (see, e.g. Hughes et al. 2013 for an observational example of this effect) and introducing environmental variations in the gas dynamical state that can influence its ability to collapse and form stars (Meidt et al. 2013; Leroy et al. 2017).

Whether the reductions in the SFE predicted in some environments by this type of model lead to reductions in the observed rate of star formation depends on the amount of fuel available for star formation. Based on the results of this work, the galaxies most likely to show signs of dynamical suppression are the nearly and fully retired class galaxies in our sample, where the spheroidal component is prominent (e.g. quenched-declining CVC area of the $W_{H_\alpha} - \beta$ relation, Figs. 4 and 6) and gas fractions are low (see also Martig et al. 2013; Gensior & Kruijssen 2021). For other systems, dynamical suppression may be less efficient because of the amount and organisation of the gas reservoir. This could explain why several of the galaxies in our sample with peaks in their CVCs (indicating a large central mass concentration or bulge) are fully star forming and why some of the galaxies in our sample that are quenched (or are approaching quenching) possess rising curves. In the first case (i.e. spaxels with $W_{H_\alpha} > 6$ Å and $\beta < 0$), it is noteworthy that galaxies with star-forming classical bulges are less massive and less concentrated than quenched systems with classical bulges (Yu et al. 2022), possibly indicating that they have a larger gas reservoir (according to the observed increase in gas fraction with decreasing stellar mass; Saintonge et al. 2017). Central star formation enhancements in classical bulges (e.g. Luo et al. 2020) could also be induced by bars (Athanassoula 1992; Wang et al. 2012, 2020) and spirals (Kim & Kim 2014; Yu et al. 2022). In the second case (i.e. spaxels with $W_{H_\alpha} < 3$ Å and $\beta > 0$), it may be relevant that anaemic spirals and S0s are disc galaxies that can have rising CVCs and no star formation (Kormendy & Bender 2012). Therefore, environmental quenching mechanisms may preferentially remove the gas from galaxies with rising CVCs,

stopping their star formation. Spirals could also fade away as the gas fraction decreases (Yu et al. 2021) and becomes S0s (Kormendy & Bender 2012).

In summary, our results show that the largest number of spaxels comes from the two extreme quenching stages: star-forming and fully retired classes (corresponding to late-type spirals and elliptical galaxies, respectively) for which $V_c$ and $\beta$ spaxel distribution coincides with the dynamical suppression hypothesis: the non-quenching or quenching of the galaxies depends on the absence or presence of a bulge or spheroid, respectively (which corresponds to low and high velocities in the $W_{H_\alpha} - V_c$ relation or rising and declining CVC in the $W_{H_\alpha} - \beta$ relation, respectively). On the other hand, the scatter analysis indicates that the presence of a classical bulge is not the only necessary condition. It seems that galaxies need to also have: higher central density (approximately above $10^{10}\, M_\odot\, \mathrm{kpc}^{-2}$), no bar, and early-type morphology (meaning no tight and prominent spiral arms).

Future work will explore the cold-gas content of the studied systems (Kalinova et al., in prep.) and will provide a complementary perspective in terms of the dynamics and mechanisms responsible for the formation of the various quenching stages of the nearby galaxies.

# References

Abadi, M. G., Moore, B., & Bower, R. G. 1999, MNRAS, 308, 947
Alam, S., Albareti, F. D., Allende Prieto, C., et al. 2015, ApJS, 219, 12
Astropy Collaboration (Price-Whelan, A. M., et al.) 2018, AJ, 156, 123
Athanassoula, E. 1992, MNRAS, 259, 345
Balogh, M. L., Navarro, J. F., & Morris, S. L. 2000, ApJ, 540, 113
Belfiore, F., Maiolino, R., Maraston, C., et al. 2016, MNRAS, 461, 3111
Birnboim, Y., & Dekel, A. 2003, MNRAS, 345, 349
Bluck, A. F. L., Maiolino, R., Piotrowska, J. M., et al. 2020a, MNRAS, 499, 230
Bluck, A. F. L., Maiolino, R., Sánchez, S. F., et al. 2020b, MNRAS, 492, 96
Cappellari, M. 2008, MNRAS, 390, 71
Cheung, E., Faber, S. M., Koo, D. C., et al. 2012, ApJ, 760, 131
Colling, C., Hennebelle, P., Geen, S., Iffrig, O., & Bournaud, F. 2018, A&A, 620, A21
Colombo, D., Kalinova, V., Utomo, D., et al. 2018, MNRAS, 475, 1791
Colombo, D., Sanchez, S. F., Bolatto, A. D., et al. 2020, A&A, 644, A97
Corcho-Caballero, P., Casado, J., Ascasibar, Y., & García-Benito, R. 2021, MNRAS, 507, 5477
Croton, D. J., Springel, V., White, S. D. M., et al. 2006, MNRAS, 365, 11
Davis, T. A., Young, L. M., Crocker, A. F., et al. 2014, MNRAS, 444, 3427

Di Matteo, T., Springel, V., & Hernquist, L. 2005, Nature, 433, 604
Dobbs, C., & Baba, J. 2014, PASA, 31, e035
Ellison, S. L., Thorp, M. D., Lin, L., et al. 2020, MNRAS, 493, L39
Emsellem, E., Monnet, G., & Bacon, R. 1994, A&A, 285, 723
Faber, S. M., Willmer, C. N. A., Wolf, C., et al. 2007, ApJ, 665, 265
Falcón-Barroso, J., Lyubenova, M., van de Ven, G., et al. 2017, A&A, 597, A48
Farouki, R., & Shapiro, S. L. 1981, ApJ, 243, 32
García-Benito, R., Zibetti, S., Sánchez, S. F., et al. 2015, A&A, 576, A135
Gensior, J., & Kruijssen, J. M. D. 2021, MNRAS, 500, 2000
Gensior, J., Kruijssen, J. M. D., & Keller, B. W. 2020, MNRAS, 495, 199
Genzel, R., Förster Schreiber, N. M., Lang, P., et al. 2014, ApJ, 785, 75
Gunn, J. E., Gott, J., & Richard, I. 1972, ApJ, 176, 1
Harris, C. R., Millman, K. J., van der Walt, S. J., et al. 2020, Nature, 585, 357
Hughes, A., Meidt, S. E., Colombo, D., et al. 2013, ApJ, 779, 46
Hunter, J. D. 2007, Comput. Sci. Eng., 9, 90
Husemann, B., & Harrison, C. M. 2018, Nat. Astron., 2, 196
Husemann, B., Jahnke, K., Sánchez, S. F., et al. 2013, A&A, 549, A87
Kalinova, V., Colombo, D., Rosolowsky, E., et al. 2017, MNRAS, 469, 2539
Kalinova, V., Colombo, D., Sánchez, S. F., et al. 2021, A&A, 648, A64
Khoperskov, S., Haywood, M., Di Matteo, P., Lehnert, M. D., & Combes, F. 2018, A&A, 609, A60
Kim, Y., & Kim, W.-T. 2014, MNRAS, 440, 208
Kormendy, J., & Bender, R. 2012, ApJS, 198, 2
Kormendy, J., & Kennicutt, R. C., Jr 2004, ARA&A, 42, 603
Kowalski, C. J. 1972, J. R. Stat. Soci. Ser. C (Appl. Stat.), 21, 1
Krumholz, M. R., & Kruijssen, J. M. D. 2015, MNRAS, 453, 739
Lacerda, E. A. D., Cid Fernandes, R., Couto, G. S., et al. 2018, MNRAS, 474, 3727
Lacerda, E. A. D., Sánchez, S. F., Cid Fernandes, R., et al. 2020, MNRAS, 492, 3073
Larson, R. B., Tinsley, B. M., & Caldwell, C. N. 1980, ApJ, 237, 692
Leroy, A. K., Walter, F., Brinks, E., et al. 2008, AJ, 136, 2782
Leroy, A. K., Schinnerer, E., Hughes, A., et al. 2017, ApJ, 846, 71
Liu, L., Bureau, M., Blitz, L., et al. 2021, MNRAS, 505, 4048
Luo, Y., Faber, S. M., Rodríguez-Puebla, A., et al. 2020, MNRAS, 493, 1686
Martig, M., Bournaud, F., Teyssier, R., & Dekel, A. 2009, ApJ, 707, 250
Martig, M., Crocker, A. F., Bournaud, F., et al. 2013, MNRAS, 432, 1914
Meidt, S. E., Schinnerer, E., García-Burillo, S., et al. 2013, ApJ, 779, 45
Meidt, S. E., Leroy, A. K., Rosolowsky, E., et al. 2018, ApJ, 854, 100
Meidt, S. E., Glover, S. C. O., Kruijssen, J. M. D., et al. 2020, ApJ, 892, 73
Monnet, G., Bacon, R., & Emsellem, E. 1992, A&A, 253, 366
Moore, B., Katz, N., Lake, G., Dressler, A., & Oemler, A. 1996, Nature, 379, 613
Peng, Y.-J., Lilly, S. J., Kovač, K., et al. 2010, ApJ, 721, 193
Romeo, A. B., & Fathi, K. 2015, MNRAS, 451, 3107
Romeo, A. B., & Fathi, K. 2016, MNRAS, 460, 2360
Romeo, A. B., & Mogotsi, K. M. 2017, MNRAS, 469, 286
Saintonge, A., Catinella, B., Tacconi, L. J., et al. 2017, ApJS, 233, 22
Salpeter, E. E. 1955, A&A, 121, 161
Sánchez, S. F., Kennicutt, R. C., Gil de Paz, A., et al. 2012, A&A, 538, A8
Sánchez, S. F., Rosales-Ortega, F. F., Iglesias-Páramo, J., et al. 2014, A&A, 563, A49
Sánchez, S. F., García-Benito, R., Zibetti, S., et al. 2016a, A&A, 594, A36
Sánchez, S. F., Pérez, E., Sánchez-Blázquez, P., et al. 2016b, Rev. Mex. Astron. Astrofis., 52, 21
Sánchez, S. F., Pérez, E., Sánchez-Blázquez, P., et al. 2016c, Rev. Mex. Astron. Astrofis., 52, 171
Savitzky, A., & Golay, M. J. E. 1964, Anal. Chem., 36, 1627
Singh, R., van de Ven, G., Jahnke, K., et al. 2013, A&A, 558, A43
Sormani, M. C., Binney, J., & Magorrian, J. 2015, MNRAS, 449, 2421
Strateva, I., Ivezić, Ž., Knapp, G. R., et al. 2001, AJ, 122, 1861
Toomre, A. 1964, ApJ, 139, 1217
Virtanen, P., Gommers, R., Oliphant, T. E., et al. 2020, Nat. Methods, 17, 261
Walcher, C. J., Wisotzki, L., Bekeraité, S., et al. 2014, A&A, 569, A1
Wang, J., Kauffmann, G., Overzier, R., et al. 2012, MNRAS, 423, 3486
Wang, J., Athanassoula, E., Yu, S.-Y., et al. 2020, ApJ, 893, 19
Yu, S.-Y., Ho, L. C., & Wang, J. 2021, ApJ, 917, 88
Yu, S.-Y., Xu, D., Ho, L. C., Wang, J., & Kao, W.-B. 2022, A&A, 661, A98
Zwillinger, D., & Kokoska, S. 1999, CRC Standard Probability and Statistics Tables and Formulae (CRC Press)

# Appendix A: Circular velocity curves across quenching stage

In the left panels of Figs. A.1 and A.2, we show the individual circular velocity curves (CVCs) of the galaxies and the normalised CVCs (with respect to the asymptotic veloc-ity) per quenching group, respectively. The right panels of the figures present the median and percentile (25th and 75th) profiles of the CVCs. The median CVCs and their percentile profiles are smoothed through the Savitzky-Golay smoothing filter (Savitzky & Golay 1964) by adopting a third-degree polynomial and a 21-point wide sliding window.
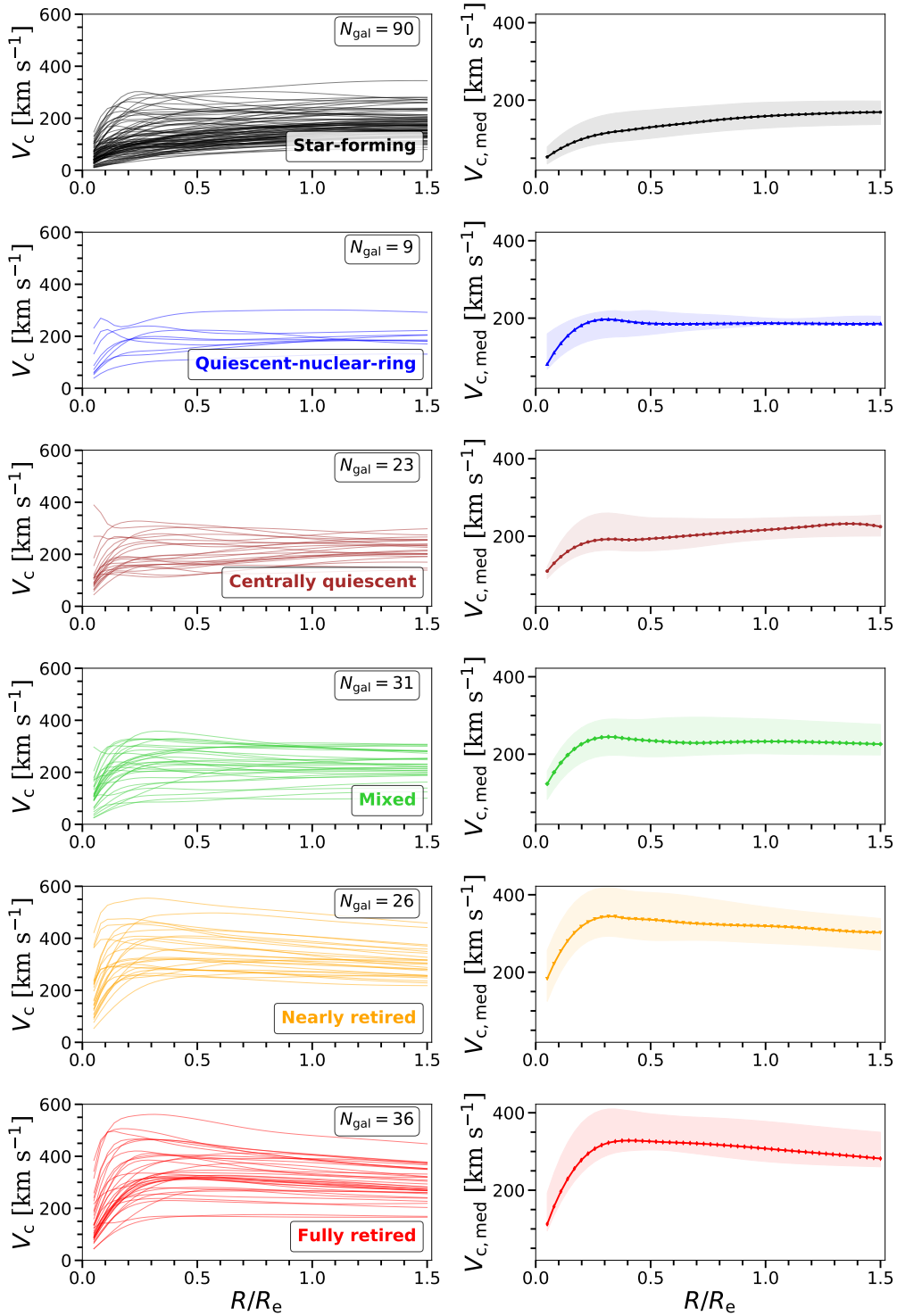


**Fig. A.1.** Circular velocity curves of our sample (thin coloured lines in the left row panels), grouped into the six quenching stages as defined in K21. The median circular velocity curve (thick coloured lines) for each quenching group is shown in the right row of panels.
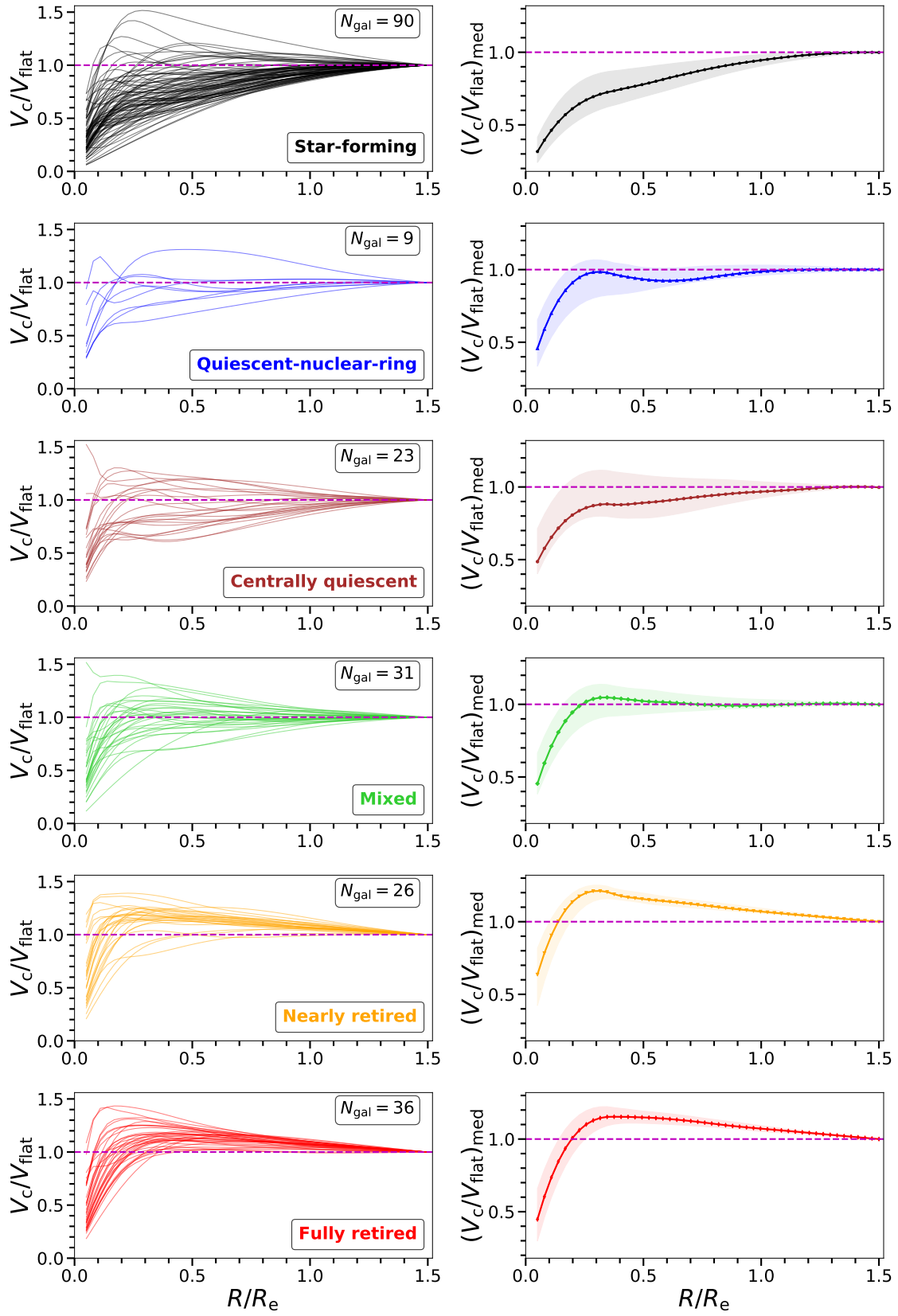
**Fig. A.2.** Normalised circular velocity profiles. *Left panels:* Circular velocity profiles, normalised with respect to the asymptotic velocity (thin coloured lines), grouped into the six quenching stages as defined in K21. *Right panels:* The median smoothed curve of the circular velocity profiles, normalised with respect to the asymptotic velocity (thick coloured lines) for each quenching group. The shadowed regions indicate the dispersion of the curves from the median value. The magenta horizontal line indicates the unity value between the two velocities.

## Appendix B: Individual $W_{H_\alpha} - V_c$ and $W_{H_\alpha} - \beta$ distribution per quenching stage

Figures B.1 and B.2 present the individual spaxel distribution of the resolved relationships $W_{H_\alpha} - V_c$ and $W_{H_\alpha} - \beta$ for each

of the six quenching stages, respectively. We compared each of these distributions with the global distribution of the relationships, consisting of the spaxels of all quenching stages.
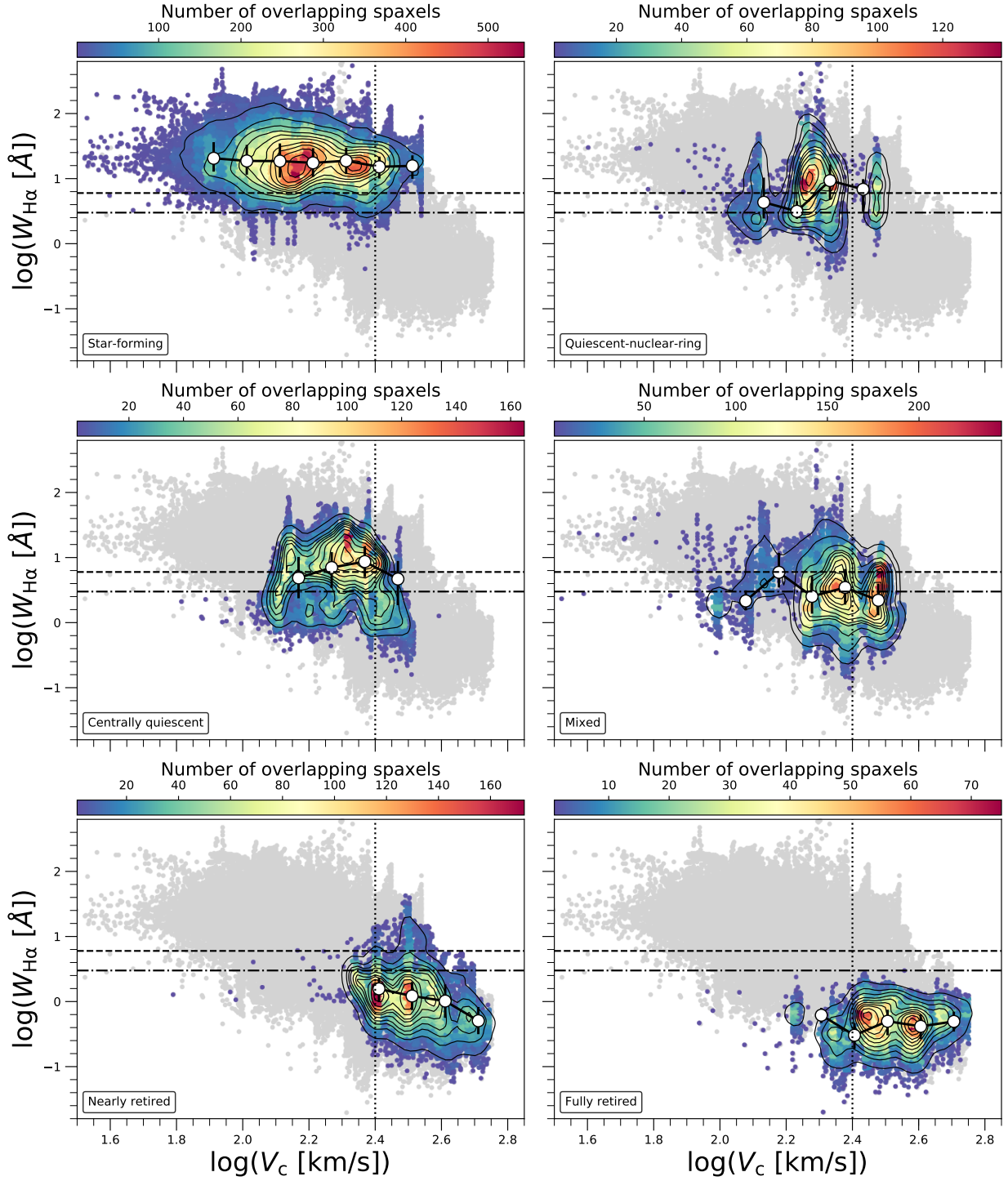


**Fig. B.1.** Resolved $W_{H_\alpha} - V_c$ scaling relation across quenching stages. Symbols and conventions follow Fig. 3. Grey dots indicate the location of all data points in the sample.
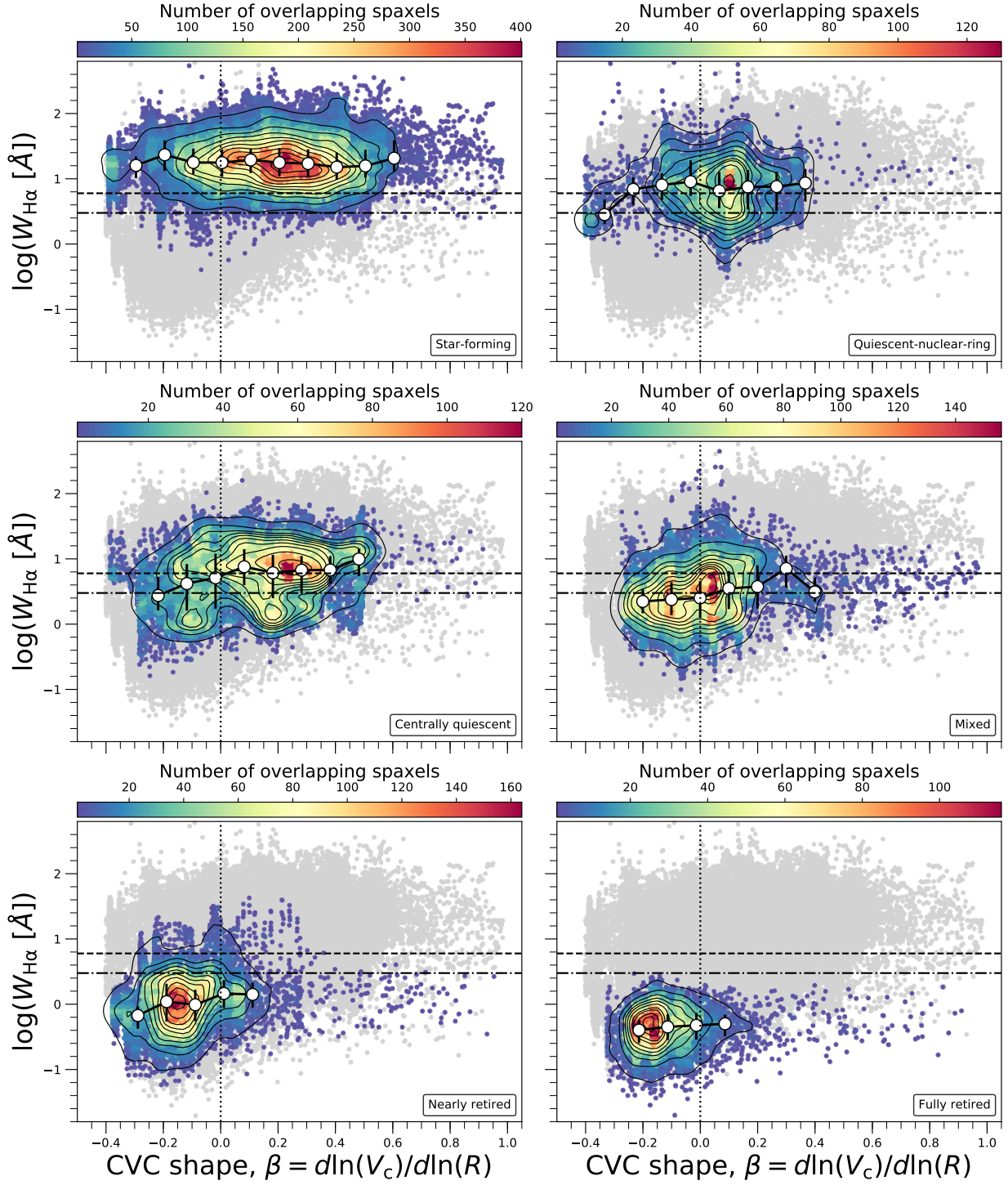
**Fig. B.2.** Resolved $W_{H\alpha} - \beta$ scaling relation across quenching stages. Symbols and conventions follow Fig. 4. Grey dots indicate the location of all data points in the sample.

## Appendix C: Stability of the $W_{H_\alpha} - V_c$ and $W_{H_\alpha} - \beta$ relations

Both resolved relationships $W_{H_\alpha} - V_c$ and $W_{H_\alpha} - \beta$ show overall stability after verification with a cross-validation technique. We randomly selected a subsample of ten galaxies from each quenching stage group (in order to keep the balance between star-forming and quenched systems) from the original data set, and reconstructed the two relationships via 100 realisations (i.e. 60 galaxies in total for each realisation) as shown in Fig. C.1.

Furthermore, we test whether there is a significant contribution from the bulge region to a certain area in the $W_{H_\alpha} - V_c$ and $W_{H_\alpha} - \beta$ relations (especially in the quenching regions due to the expected act of the dynamical suppression mechanism). Interestingly, the stability of the spaxel distribution of the relationships is preserved in both cases when the spaxels of the galaxies are taken into account with or without the central regions (i.e. below and above 0.5 $R_e$, respectively) as presented in Fig. C.2. This shows that the central spaxels of the galaxies are not necessary contributing to any specific area in the global relationships (or to a certain quenching area).
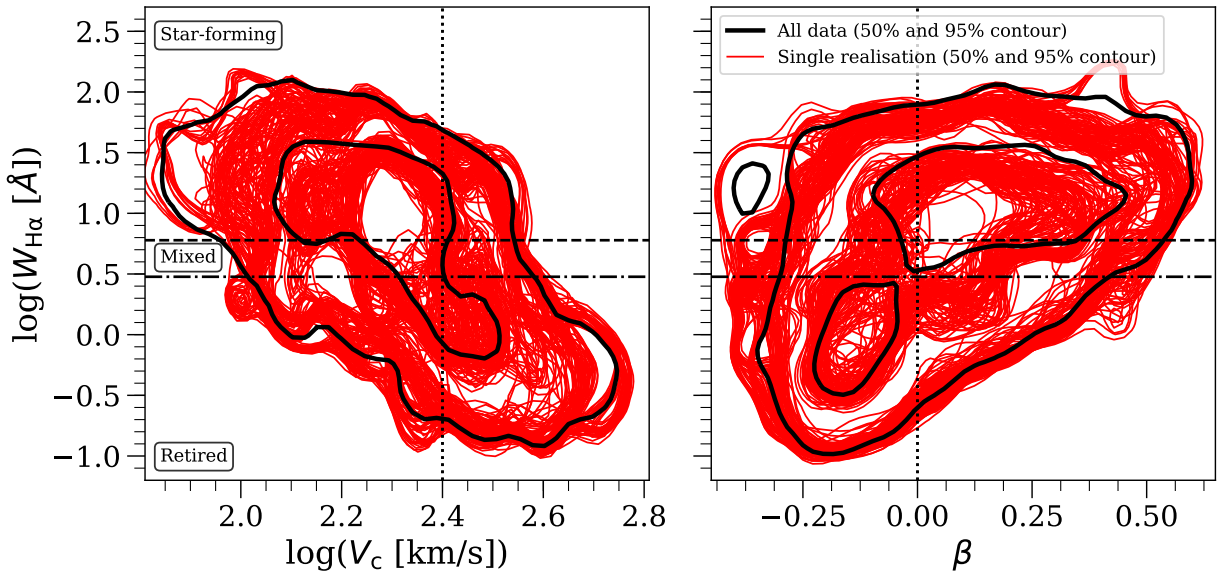


**Fig. C.1.** Testing the stability of the resolved scaling relations ($W_{H_\alpha} - V_c$, left; $W_{H_\alpha} - \beta$, right) through a cross-validation technique. The red lines indicate the spaxels of 60 randomly selected galaxies from the original data set (where 10 galaxies from each of the 6 quenching stages are chosen) for 100 single realisations. The inner and the outer contours represent the relationships constructed with 50% and 95% of the spaxel distribution, respectively, of the full sample of 215 galaxies (black contours) and each subsample of 60 galaxies (red contours). Both relationships overall show stability regarding the studied sample across quenching stage.
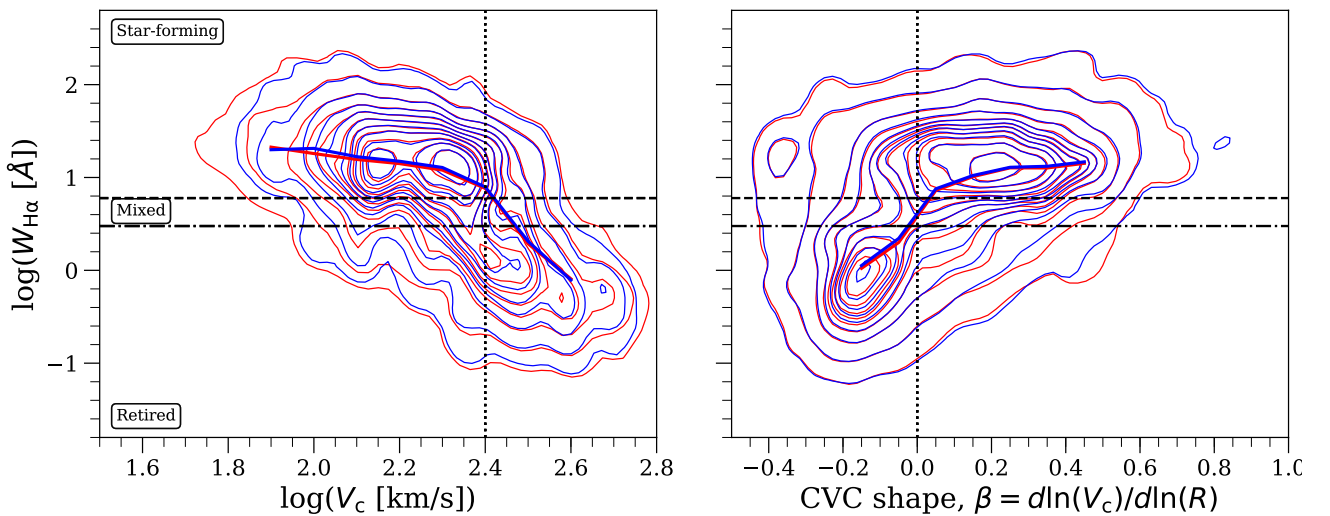


**Fig. C.2.** Resolved scaling relations ($W_{H_\alpha} - V_c$, left; $W_{H_\alpha} - \beta$, right) for all data in the sample ($R/R_e > 0$, red contours) and for data where $R/R_e > 0.5$ (blue contours). With the same colours, full lines indicate the running $W_{H_\alpha}$ related to the quantity on the $x$−axis for the given group.